

Proceedings of the Research Institute of Atmospherics,
Nagoya University, vol. 24 (1977)

PHASE ERROR MEASUREMENT AND CORRECTION IN 8-CM RADIOHELIOGRAPH

Noboru SUZUKI

Abstract

A computer program to improve dirty solar maps on the basis of measured phase errors was developed for the 8-cm radioheliograph at Toyokawa. The radioheliograph is a simple T-shaped phase-switching interferometer, and is not equipped with a phase-lock system. Therefore we use a conventional method of phase measurement observing the sun itself as a calibrating source. A dirty map is Fourier transformed to correct phase errors in the (u,v) plane. A clean map is obtained after the inverse transform of the corrected Fourier components. The procedure for the phase correction is given in this paper. Some examples of results of the phase correction are also illustrated.

1. Introduction

* The 8-cm radioheliograph at Toyokawa (Ishiguro et al., 1975) has been in operation since June 1975. The radioheliograph is a T-shaped array of 3-m dishes and consists of 32 elements in the E-W direction and of 17 elements in the N-S direction. The signals from the 32 E-W elements and from the 16 elements are independently transmitted to the phase center, where these signals are phase switched and synchronously detected to obtain a pencil beam. The HPBW of the pencil beam is $2'25(E-W) \times 2'25 \sec ZD(N-S)$ after smoothing, where ZD represents the ze-

nith distance of the sun. A solar map observed by the radioheliograph is represented by a grid of 64x64 picture points and covers the field of view of 40'x40'secZD. In the Fourier transformed domain, which we call hereafter as the (u,v) plane, 32x16 independent Fourier components of the brightness distribution are observed. Each observed Fourier component is represented by amplitude and phase data.

The performance of the radioheliograph is usually sensitive to phase errors rather than amplitude errors. The phase errors cause unexpected sidelobe patterns around the local maximum of brightness in the map. These enhancements or depressions may be sometimes mistaken for active regions or coronal holes. Therefore phase correction is of fundamental importance in order to obtain good solar maps.

We have no active phase-lock or phase-calibration systems, so we must look for a passive way of phase measurement. If the telescope has a sufficient sensitivity and phase stability, phase errors are calibrated by observing a point-like radio source. Scanning a point source yields a mirror image of the actual beam pattern, and phase errors can be calculated through its Fourier transform (Peckham, 1973).

Ishiguro (1971, 1974) developed a phase correction method through data processing by combining both one-dimensional compound- and grating-interferometric data. By his method, phase errors for the antenna (see Fig. 1) are determined with a good accuracy. This method can be extended to the two-dimensional T-shaped array. For this purpose, an additional antenna is placed at the phase center of the array to estimate phase errors along the three arms of the array near the phase center.

We can also measure phase errors by pointing an antenna together with an adjacent antenna on the same baseline to the sun, and measuring the shift of a recorded image from its correct position. It takes about two hours to attain all the calibration of 32 antennas in the E-W direction. The measurement needs so much time that we can not do this frequently. We have used, however, this method.

The phase correction is performed by adjusting the relative angle of the rotary phase shifters (Tanaka et al., 1970). But the maps observed before the correction must be corrected by an image processing. The most common and fundamental way is to correct errors in the (u,v) plane. We developed a computer program to improve dirty maps, based on this principle. Computer plays an important role in the image correction. A particular attention is paid to reduction of the size of necessary core storage and of computing time. A useful algorithm of the Fourier

transform for the T-shaped array is also described here.

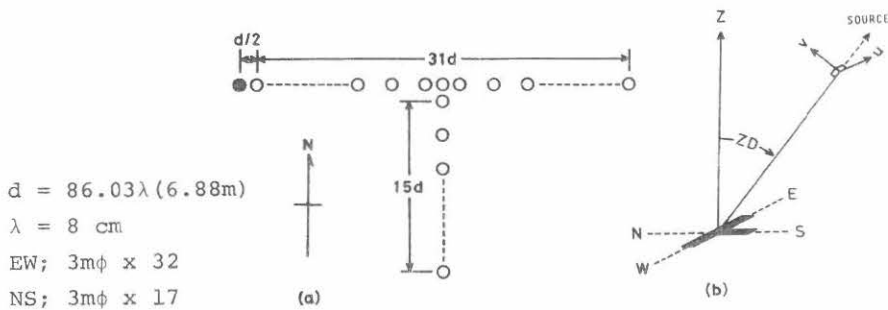


Fig. 1 (a) Configuration and size of array.
The shaded antenna is one of the auxiliary antennas for the one-dimensional compound interferometer.
(b) The coordinate system.

2. Theory

2. 1 Basic Theory

It is assumed here that the radioheliograph has no amplitude errors and that observation is made at the central meridian.

Let a phase error of signals from a k -th antenna be ϕ_k , then the far-field distribution for the N -element array is given by

$$e(x) = \sum_{k=1}^N \exp[j\{2\pi(2k-1)\Delta u x + \phi_k\}] \quad (1)$$

with $x = \sin \theta$,

$$\Delta u = d/(2\lambda), \quad (\text{for E-W array})$$

where the origin of the coordinate u is placed at the (phase) center of the E-W array (see Fig. 1), and θ represents the incident angle measured from the plane perpendicular to the baseline of the array. d and λ represent the unit spacing and operating wavelength respectively.

By using Dirac's delta function, the aperture illumination function is expressed as follows:

$$E(u) = \sum_{k=1}^N \delta\{u - (2k-1)\Delta u\} \exp(j\phi_k) \quad (2)$$

Let phase-lag errors between the phase center and antennas on east, west and south arm be ϕ_m^E , ϕ_m^W and ϕ_n^S , where m and n are antenna numbers counted from the phase center. From Eq. (2), the aperture illumination function for E-W and N-S direction are expressed as follows:

$$\left. \begin{aligned} G(u,v) &= \left[\sum_{m=1}^N \delta\{u - (2m-1)\Delta u\} \exp(j\phi_m^E) \right. \\ &\quad \left. + \sum_{m=1}^N \delta\{u + (2m-1)\Delta u\} \exp(j\phi_m^W) \right] \delta(v) , \\ H(u,v) &= \left[\sum_{n=1}^N \delta\{v + (2n-1)\Delta v\} \exp(j\phi_n^S) \right] \delta(u) , \end{aligned} \right\} (3)$$

where $\Delta u = d/(2\lambda)$ and $\Delta v = (d/(2\lambda)) \cos ZD$.

The power pattern $p(x,y)$ produced by E-W and N-S array is expressed as

$$\begin{aligned} p(x,y) &= \{[g(x,y) + h(x,y)]\{g(x,y) + h(x,y)\}^* \\ &\quad - [g(x,y) - h(x,y)]\{g(x,y) - h(x,y)\}^*\}/4 \\ &= \{g(x,y)h(x,y)^* + g(x,y)^*h(x,y)\}/2 , \end{aligned} \quad (4)$$

where $g(x,y) = F\{G(u,v)\}$, $h(x,y) = F^{-1}\{H(u,v)\}$, and $*$ denotes complex conjugate. $F\{f\}$ means the Fourier transform of f ; and $F^{-1}\{f\}$, its inverse transform.

Therefore,

$$P(u,v) = \{P'(u,v) + P'(-u,-v)^*\}/2 , \quad (5)$$

where

$$P'(u,v) = \iint_{-\infty}^{\infty} G(u',v')H(u'-u,v'-v)du'dv'. \quad (6)$$

From Eqs. (3) and (6),

$$P'(u,v) = \sum_{m=1}^N \sum_{n=1}^N [\delta\{u - (2m-1)\Delta u, v + (2n-1)\Delta v\}C(2m-1,1-2n) + \delta\{u + (2m-1)\Delta u, v + (2n-1)\Delta v\}C(1-2m,1-2n)] \quad (7)$$

with $C(2m-1,1-2n) = \exp\{j(\phi_m^E - \phi_n^S)\}$,

$$C(1-2m,1-2n) = \exp\{j(\phi_m^W - \phi_n^S)\} , \quad \left(\begin{array}{l} m=1,2,\dots,N \\ n=1,2,\dots,N \end{array} \right) .$$

From Eq. (7), it can be said that $P(u,v)$ has only odd Fourier components.

Scanning a source whose brightness distribution is $t_s(x,y)$, we get $t_{\text{obs}}(x,y)$ expressed as follows:

$$t_{\text{obs}}(x,y) = \iint_{-\infty}^{\infty} t_s(x',y')p(x'-x,y'-y)dx'dy', \quad (8)$$

thus,

$$T_{\text{obs}}(u,v) = T_s(u,v)P(u,v) , \quad (9)$$

where

$$F\{t_{\text{obs}}(x,y)\} = T_{\text{obs}}(u,v) ,$$

$$F\{t_s(x,y)\} = T_s(u,v) .$$

2. 2 Procedure for Phase Correction

The left-hand side and the right-hand side of Eq. (9) can be expressed as follows each;

$$T_{\text{Obs}}(u,v) = \sum_{m=1-N}^N \sum_{n=1-N}^N [\delta\{u - (2m-1)\Delta u, v - (2n-1)\Delta v\} \\ \times C_{\text{Obs}}(2m-1, 2n-1)] , \quad (10)$$

$$T_{\text{S}}(u,v)P(u,v) = \sum_{m=1-N}^N \sum_{n=1-N}^N [\delta\{u - (2m-1)\Delta u, v - (2n-1)\Delta v\} \\ \times T_{\text{S}}\{(2m-1)\Delta u, (2n-1)\Delta v\}C(2m-1, 2n-1)] . \quad (11)$$

Comparing the coefficients of Eqs. (10) and (11), we obtain

$$C_{\text{Obs}}(2m-1, 2n-1) = T_{\text{S}}\{(2m-1)\Delta u, (2n-1)\Delta v\}C(2m-1, 2n-1) . \quad (12)$$

When $C(2m-1, 2n-1)$ is known, from Eq. (12),

$$T_{\text{S}}\{(2m-1)\Delta u, (2n-1)\Delta v\} = C_{\text{Obs}}(2m-1, 2n-1)/C(2m-1, 2n-1) \\ = C_{\text{Obs}}(2m-1, 2n-1)C(2m-1, 2n-1)^* . \quad (13)$$

Let $T_{\text{S}}(u,v)$ obtained by Eq. (13) be $T_{\text{C}}(u,v)$ for distinction between true $T_{\text{S}}(u,v)$ and that after phase correction. Then,

$$T_{\text{C}}(u,v) = \sum_{m=1-N}^N \sum_{n=1-N}^N [\delta\{u - (2m-1)\Delta u, v - (2n-1)\Delta v\} \\ \times C_{\text{Obs}}(2m-1, 2n-1)C(2m-1, 2n-1)^*] . \quad (14)$$

Therefore the brightness distribution after the phase correction, $t_{\text{C}}(x,y)$, is given by

$$t_{\text{C}}(x,y) = F^{-1}\{T_{\text{C}}(u,v)\} . \quad (15)$$

2. 3 Procedure for Phase Error Measurement

Let the field distribution of the adding interferometer composed of a k-th and a (k+1)-th antenna of the east arm be $e_{k,k+1}$,

$$\begin{aligned}
 e_{k,k+1} &= \exp[j\{2\pi(2k-1)\Delta u x + \phi_k^E + \phi_k\}] \\
 &\quad + \exp[j\{2\pi(2k+1)\Delta u x + \phi_{k+1}^E + \phi_{k+1}\}] , \\
 &\quad (k=1,2,\dots,N-1) . \quad (16)
 \end{aligned}$$

with $\phi_k = 2\pi f_k(t - t_0)$, where f_k is the rotary phase shifter speed, t is the observation time, and t_0 is the time when the grating beam of k-th and (k+1)-th antenna system passes the central meridian. The power pattern is given by

$$\begin{aligned}
 P_{k,k+1} &= e_{k,k+1} e_{k,k+1}^* / 4 \\
 &= \{1 + \cos(2\pi K)\} / 2 , \quad (17)
 \end{aligned}$$

$$\text{where } K = \Delta u x + f_s(t - t_0) + \phi_k^E , \quad (18)$$

$$\begin{aligned}
 f_s &= f_{k+1} - f_k , \\
 \Delta\phi_k^E &= (\phi_{k+1}^E - \phi_k^E) / (2\pi) \quad (19)
 \end{aligned}$$

If the maximum on the record appears at $t = t_1$, from Eq. (18), $\Delta\phi_k^E$ is given by

$$\Delta\phi_k^E = K - \Delta u x - f_s(t_1 - t_0) . \quad (20)$$

Here, $\Delta\phi_k^E$ expresses the phase error of k-th and (k+1)-th antenna system. Since x is expressed by declination (δ) and hour angle (H) of the sun as

$$x = \cos\delta \sin H ,$$

with H of a linear function of time, we can calculate the value of x at time t_1 . It is clear from Eq. (17) that $p_{k,k+1}$ has the maxima for K of any integer. We select it so that $|\Delta\phi_k^E| \leq 0.5$. Thus the phase error $\Delta\phi_k^E$ is determined from Eq. (20).

Eq. (19) gives ϕ_{k+1}^E as

$$\phi_{k+1}^E = 2\pi \sum_{i=1}^k \Delta\phi_i^E + \phi_1^E, \quad (k=1,2,\dots,N-1) . \quad (21)$$

Therefore all the phase errors can be relatively calibrated except ϕ_1^E , ϕ_1^W and ϕ_1^S in the same way, but

$$x = \sin\gamma \cos\delta \cos H - \cos\gamma \sin\delta$$

for the N-S array, where γ is the latitude at the phase center. ϕ_1^E , (or ϕ_1^W) and ϕ_1^S must be determined by other method which will be described in the following section.

3. The Data Processing Which Has Been Used

The old data processing of the 8-cm radioheliograph (Tanaka et al., 1970; Arisawa, 1971; Shibasaki et al., 1976) can be divided into nine parts as follows. It is assumed here that $\Delta\phi_k^E, \Delta\phi_k^W, \Delta\phi_k^S = 0$ ($k=1,2,\dots,N-1$).

- (1) Removal of DC drift from original data.
- (2) Rearrangement of picture points to a correct order.
- (3) Removal of Fourier components beyond the spatial resolution of the array.
- (4) Correction of phase errors among three arms of the T-shaped array to equalize the background level at the edge of the map by an iterative method. ϕ_1^E, ϕ_1^W and ϕ_1^S in the previous section are determined by this method.
- (5) Smoothing by tapering Fourier components to reduce theoretical sidelobes to -21dB.
- (6) Correction of the weight due to the envelope pattern of the individual antennas.

- (7) Determination of the center of the image from the centroid at the half brightness of the quiet sun.
- (8) Rotation of coordinates to bring the north pole at the top.
- (9) Calibration of brightness using the simultaneous total-flux observations.

4 New Data Processing

When each antenna has a large phase error, the transformed image is distorted all the more by the processing (4) in the previous section. This effect is removed by the new procedure as will be described in the following.

Phase error data files are stored in a magnetic disk, and two-dimensional files for real and imaginary Fourier components are prepared before the processing by using the phase error data files. The phase error between east and west arm is calibrated by the same method described in the Section 2. Therefore either ϕ_1^E or ϕ_1^W , and ϕ_1^S are unknown. The phase offset of the E-W array from the phase center of the T-shaped array is supposed to be the central value of the fitting line for the phase errors of the array; examples of a fitting line are displayed in Fig. 2. After the phase correction is carried out according to Eq. (14) and (15), the phase errors between the three arms and the phase center are finally determined by the processing (4).

The Fourier transform of an map composed of $64 \times 64 = 4096$ picture points requires $128 \times 128 \times 2 = 32768$ words of core storage capacity for real and imaginary parts, because the Fourier components of the map have only odd harmonics as Eq. (7) shows and the DFT is performed on the assumption that one cycle of a picture to transform is composed of 128×128 picture points; the map alternates with its inverted map. An odd discrete Fourier transform (ODFT) (Vernet, 1971) is applied for saving core storage capacity and computing time (see Appendix).

5. Results and Discussion

The examples of phase error data measured by the method described in the Section 2.3, is illustrated in Fig. 2, and the results after the phase correction based on those data are shown in Fig. 4, 5 and 7. The number of dots in each picture element of the maps corresponds to brightness temperature (Shibasaki, et al., 1976).

The distorted map, shown in Fig. 3 (c), is simulated to make sure that the phase error data are usable. The phase offset of the N-S array is determined by trial and error. The original map after noise reduction by the processing (3) is shown in Fig. 3 (b). The effect of the phase errors in the beam pattern is reducing cosine components and introducing sine components, which distorts the main beam and gives an increase of the sidelobe level. The distorted beam pattern appears around small but strong sources' image. An example of the distorted map is shown in Fig. 4 (a) and (c). A depression is seen in the south-east side of the highest peak. This depression disappeared after the new procedure as shown in Fig. 4 (b) and (d).

Figs. 5 and 7 are results which are corrected by the phase error data shown in Fig. 2 (d). The phase error data only for E-W array are used in this case. Fig. 5 (a) and (c) show that the unwanted sidelobe produces a deep depression and an enhancement on one and the other side of the highest peak. Fig. 6 (a) shows the smoothed beam pattern simulated by using the phase error data; and Fig. 6 (b) the same pattern without phase errors. The depression and the enhancement on the west side of the peak disappeared after the new processing. Though the phase errors of the N-S array are not corrected, the image in the N-S direction is slightly improved, since the phase errors of the arrays in both directions are coupled in the (u,v) plane.

A solar map without active regions is shown in Fig. 7. There is an extended depression on the west side of the solar disk, as shown in Fig. 7 (a) and (c). This was believed due to phase errors, because the depression did not move with the rotation of the sun. And this map was corrected by the phase correction as we expected.

The new processing improved good amount of data observed by the radioheliograph. We can not generally say how long a set of phase data is useful for the correction from the day when the measurement was made, as the phase stability depends on a season. For example, the map shown in Fig. 5 (a) is well corrected though it had passed more than a

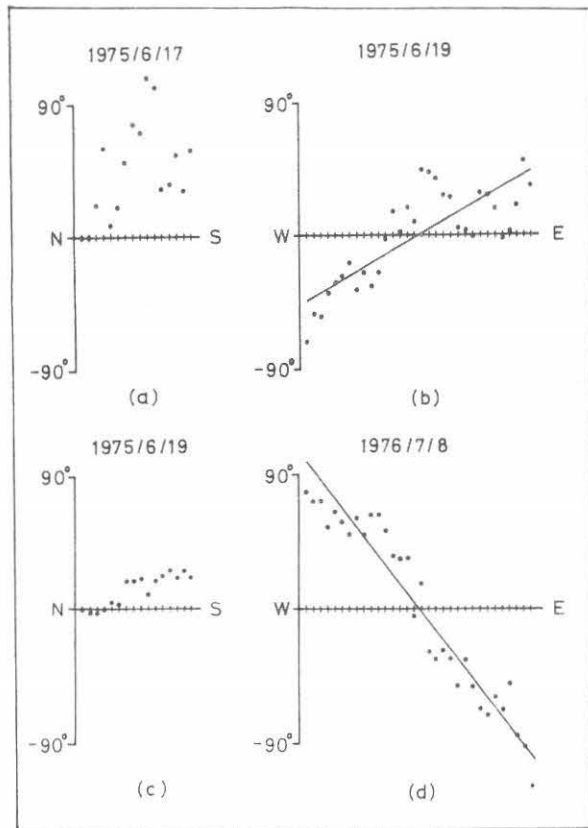


Fig. 2. Examples of the measured phase errors and the least square fitting lines for determining the phase offset of overall phase distribution along the E-W array. (c) shows the phase errors after adjusting phase shifters, based on the data (a).

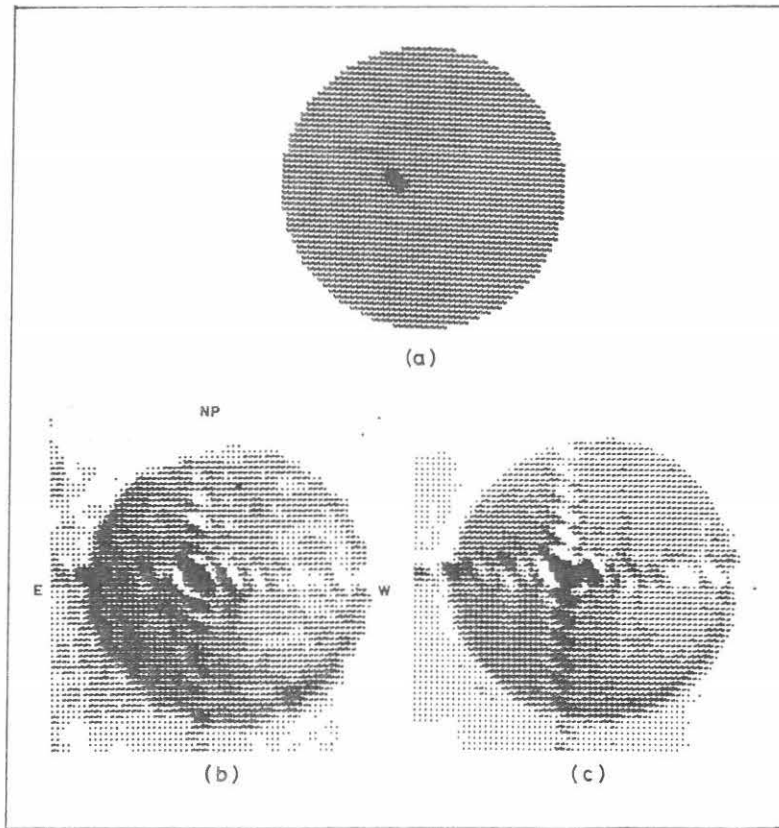


Fig. 3. A simulation of the distorted map.
 (a) The model of the solar disk used for this simulation.
 (b) The original map after noise reduction.
 (c) The simulation for (b), based on the phase error data shown in Fig. 2 (d).

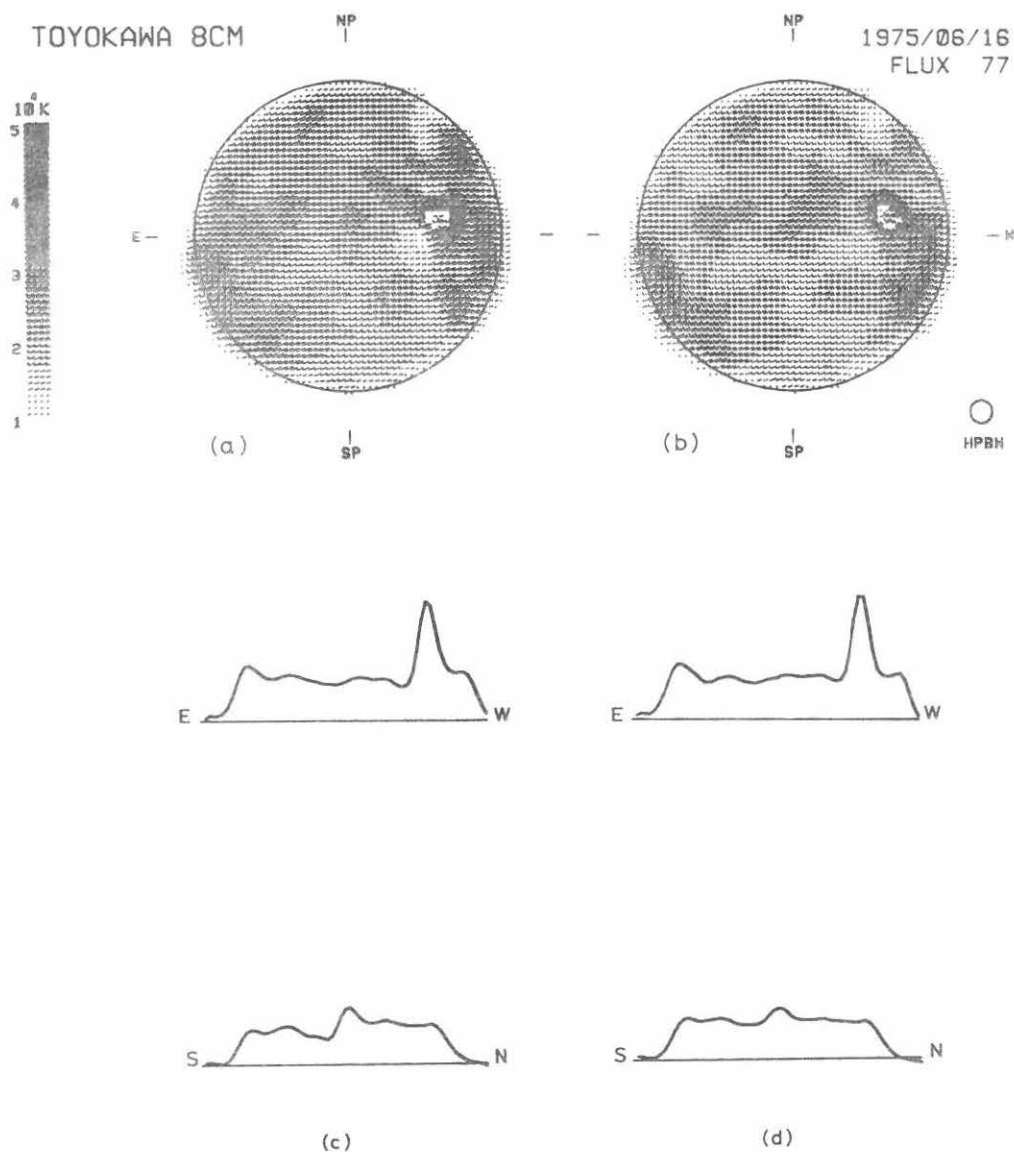


Fig. 4. An example of the phase correction.
 (a) The solar map after the old processing.
 (b) After the new processing, based on the phase error data shown in Fig. 2 (a) and (b).
 (c) The cross sections across the depression of (a).
 (d) The same cross section after the new processing.

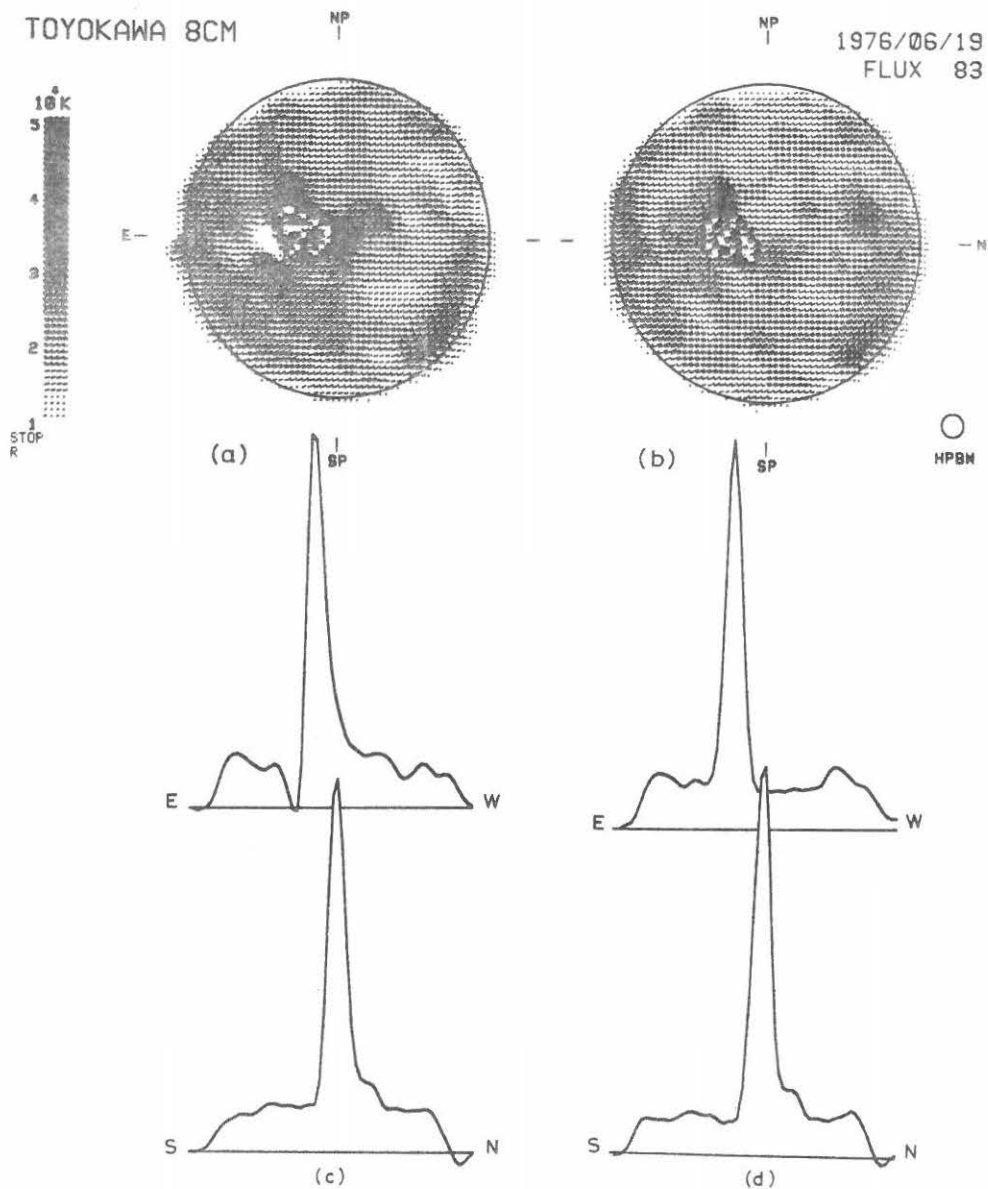


Fig. 5. An example of the phase correction.
 (a) The solar map after the old processing. The original map is shown in Fig. 3 (b).
 (b) After the new processing, based on the phase error data shown in Fig. 2 (d).
 (c) The cross section of the highest peak of (a).
 (d) The same curve for (b).

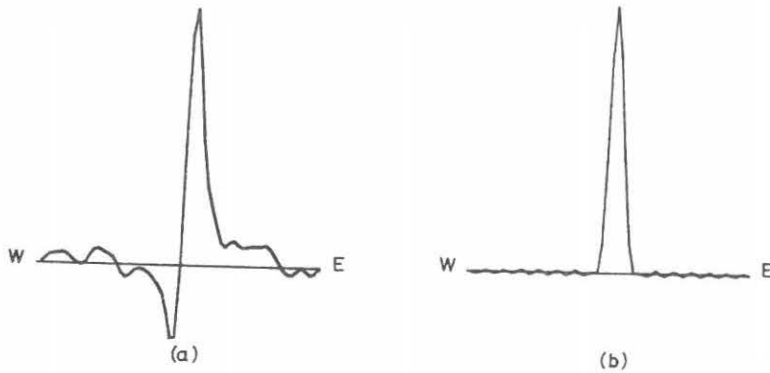


Fig. 6. (a) The cross section of the simulated beam pattern, based on the phase error data shown in Fig. 2 (d). Compare this with Fig. 5 (c).
 (b) The same curve without phase errors.

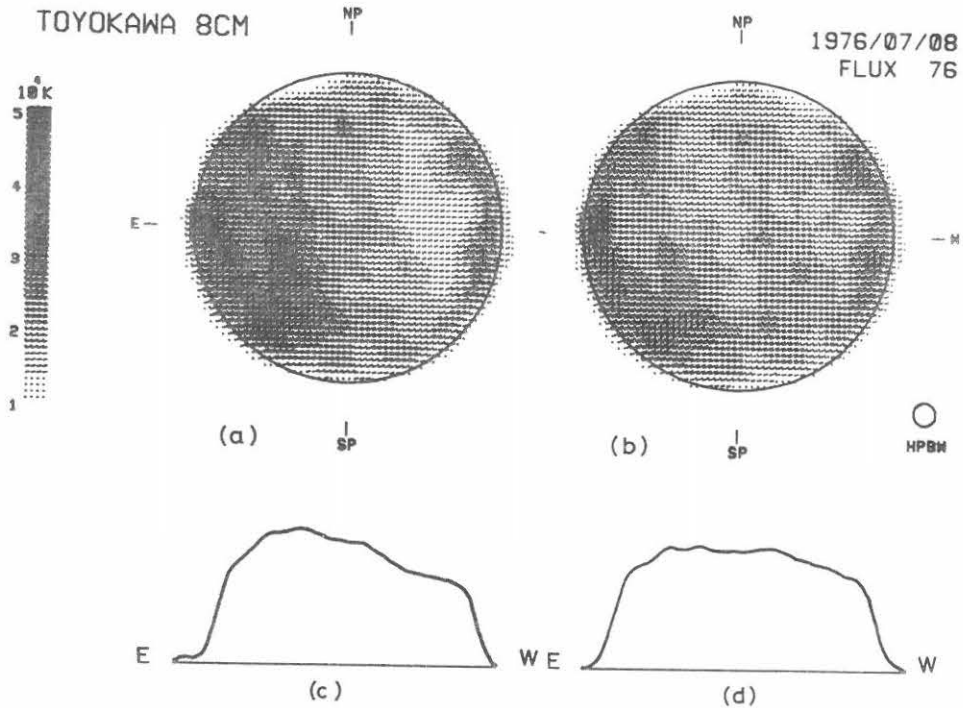


Fig. 7. An example of the phase correction.
 (a) The solar map after the old processing.
 (b) After the new processing, based on the phase error data shown in Fig. 2 (d).
 (c) The integrated profile for 64 cross sections of (b).
 (d) The same profile for (b).

month before the calibration was made, but another set of data can be used only for observation within a few days.

We can calibrate phase errors for every observation if the phase calibration system developed by Ishiguro begins to work; the new procedure can be used as it is.

Appendix

A 2N-point Fourier transform is computed with an N-point Fourier transform with an ODFT.

An one-dimensional 2N-point DFT is defined as

$$\begin{aligned}
 C_r &= \frac{1}{2N} \sum_{k=0}^{2N-1} f_k \exp\{-j2\pi rk/(2N)\} \\
 &= \frac{1}{2N} \left[\sum_{m=0}^{N-1} f_{2m} \exp\{-j2\pi r(2m)/(2N)\} \right. \\
 &\quad \left. + \sum_{m=0}^{N-1} f_{2m+1} \exp\{-j2\pi r(2m+1)/(2N)\} \right] \\
 &= \frac{1}{2N} \left\{ \sum_{m=0}^{N-1} f_{2m} \exp(-j2\pi rm/N) \right. \\
 &\quad \left. + \exp(-j\pi r/N) \sum_{m=0}^{N-1} f_{2m+1} \exp(-j2\pi rm/N) \right\} .
 \end{aligned}$$

If even harmonics has zero amplitude, C_r is written as

$$C_r = \frac{1}{2N} \left\{ \exp(-j\pi r/N) \sum_{m=0}^{N-1} f_{2m+1} \exp(-j2\pi rm/N) \right\} .$$

It is easily reduced that the spectrum composed of only odd harmonics is transformed into real signals expressed as follows:

$$C_{r+N} = -C_r , \quad (r=0,1,\dots,N-1) .$$

An inverse transform is expressed as:

$$\begin{aligned}
 f_k &= \sum_{r=0}^{2N-1} C_r \exp\{j2\pi rk/(2N)\} \\
 &= \sum_{r=0}^{N-1} C_r \exp\{j2\pi rk/(2N)\} + \sum_{r=N}^{2N-1} C_r \exp\{j2\pi rk/(2N)\} \\
 &= \sum_{r=0}^{N-1} C_r \exp\{j2\pi rk/(2N)\} + \sum_{r=0}^{N-1} (-C_r) \exp\{j2\pi(r+N)k/(2N)\} \\
 &= \sum_{r=0}^{N-1} C_r \{1 - \exp(j\pi k)\} \exp\{j2\pi rk/(2N)\} ,
 \end{aligned}$$

thus,

$$f_k = \begin{cases} f_{2m} = 0 \\ f_{2m+1} = 2 \sum_{r=0}^{N-1} \{C_r \exp(j\pi r/N)\} \exp(j2\pi rm) , \end{cases}$$

($m=0,1,\dots,N-1$) .

A two-dimensional ODFT is obtained in the same way, and the results are expressed as follows:

$$\begin{aligned}
 C_{r,s} &= \frac{1}{4N^2} \exp\{-j\pi(r+s)/N\} \\
 &\quad \times \sum_{m=0}^{N-1} \sum_{n=0}^{N-1} [f_{2m+1,2n+1} \exp\{-j2\pi(rm+sn)/N\}] , \\
 f_{2m+1,2n+1} &= 4 \sum_{r=0}^{N-1} \sum_{s=0}^{N-1} \left\{ [C_{r,s} \exp\{j\pi(r+s)/N\}] \right. \\
 &\quad \left. \times \exp\{j2\pi(rm+sn)/N\} \right\} .
 \end{aligned}$$

An ODFT is useful for one-dimensional compound interferometers and our T-shaped interferometer as they have no even harmonics, and it reduces the size of the necessary core storage capacity to 1/4 and computing time to less than 1/4, compared with those of a usual FFT.

Acknowledgements

The author wishes to express his sincere thanks to Prof. H. Tanaka of University of Tokyo and of Nagoya University for his guidance and encouragement. He also thanks Assoc. Prof. S. Enome, Mr. M. Ishiguro and Mr. K. Shibasaki of Toyokawa Observatory for their helpful discussions and criticisms. He is also grateful to Miss R. Shirai for her assistance.

Reference

- Arisawa, M.: Improved Radio Mapping of the Sun, Proc. Res. Inst. Atmospherics, Nagoya Univ., 18, 89 (1971).
- Ishiguro, M.: Image Correction in High-Resolution Radio Interferometer, Proc. Res. Inst. Atmospherics, Nagoya Univ., 18, 73 (1971).
- Ishiguro, M.: Phase Error Correction in Multi-Element Radio Interferometer by Data Processing, Astrophys. Suppl. 15, 431 (1974).
- Ishiguro, M., H. Tanaka, S. Enome, C. Torii, Y. Tsukiji, S. Kobayashi and N. Yoshimi: 8-CM Radioheliograph, Proc. Res. Inst. Atmospherics, Nagoya Univ., 22, 1 (1975).
- Peckham, R. F.: A Phase Correction Technique for Radio Link Interferometry, Mon. Not. R. astr. Soc., 165, 25, 38 (1973).
- Shibasaki, K., M. Ishiguro, S. Enome, H. Tanaka, C. Torii, Y. Tsukiji, S. Kobayashi and N. Yoshimi: λ 8-CM Radioheliograph, Proc. Res. Inst. Atmospherics, Nagoya Univ., 23, 21 (1976).
- Tanaka, H., S. Enome, C. Torii, Y. Tsukiji, S. Kobayashi, M. Ishiguro and M. Arisawa: 3-CM Radioheliograph, Proc. Res. Inst. Atmospherics, Nagoya Univ., 17, 57 (1970).
- Vernet, J. L.: Real Signals Fast Fourier Transform: Storage Capacity and Step Number Reduction by Means of An Odd Discrete Fourier Transform, Proc. IEEE Trans., 59, 1531 (1971).

